High-Fidelity Bilateral Teleoperation Systems and the Effect of Multimodal Haptics

Mahdi Tavakoli, Arash Aziminejad, Rajni V. Patel, and Mehrdad Moallem

***Abstract*—In master–slave teleoperation applications that deal with a delicate and sensitive environment, it is important to provide haptic feedback of slave/environment interactions to the user's hand as it improves task performance and teleoperation transparency (fidelity), which is the extent of telepresence of the remote environment available to the user through the master–slave system. For haptic teleoperation, in addition to a haptics-capable master interface, often one or more force sensors are also used, which warrant new bilateral control architectures while increasing the cost and the complexity of the teleoperation system. In this paper, we investigate the added benefits of using force sensors that measure hand/master and slave/environment interactions and of utilizing local feedback loops on the teleoperation transparency. We compare the two-channel and the four-channel bilateral control systems in terms of stability and transparency, and study the stability and performance robustness of the four-channel method against nonidealities that arise during bilateral control implementation, which include master–slave communication latency and changes in the environment dynamics. The next issue addressed in the paper deals with the case where the master interface is not haptics capable, but the slave is equipped with a force sensor. In the context of robotics-assisted soft-tissue surgical applications, we explore through human factors experiments whether slave/environment force measurements can be of any help with regard to improving task performance. The last problem we study is whether slave/environment force information, with and without haptic capability in the master interface, can help improve outcomes under degraded visual conditions.**

***Index Terms*—Bilateral teleoperation control, multimodal haptics, transparency.**

I. Introduction

A MASTER–SLAVE teleoperation system consists of a slave robot and a master human–machine interface (HMI) from which the human operator controls the slave and is provided with visual feedback from the slave side. In teleoperation applications that deal with a delicate and sensitive environment such as soft-tissue surgery, it is important to also provide a feedback of slave/environment contact forces (haptic feedback) to the user's hand. Such a feedback is shown to enhance human performance [1] and, in the context of a robot-assisted surgery, can improve task performance as gauged by measures such as task success rate and completion time and economy of exerting force and thus incurring trauma to tissue [2], [3]. On the other hand, the absence of a haptic feedback to the surgeon in a robot-assisted surgery is a safety concern and a cause of errors [4]. For instance, in a study that involves minimally invasive cholecystectomy, it was observed that inappropriate and excessive application of force was a main cause of perforation of the gall bladder [5]. Such a safety concern is particularly significant if visual feedback to the surgeon is degraded, e.g., if fluids from the patient's body cloud the camera lens, or the instruments leave the limited field of view of the endoscopic camera.

For haptic teleoperation, the minimum requirement is to have a force-reflective HMI, in which case it is possible to reflect slave/environment interaction forces to the user's hand merely based on the difference between the master and the slave positions and without measurement of the slave/environment or the hand/master contact forces. However, compared to such a "position-error-based" method, the fidelity and the reliability of the haptic teleoperation can be enhanced if the bilateral controller is fed with the measurements of master-side and/or slave-side force sensors. Therefore, the first issue addressed in this paper (Section II) is the extent of benefits added by one or more force sensors and the effects of a bilateral control structure on teleoperation stability and transparency, which can be compromised due to the implementation issues and changes in the environment dynamics. We also study the effect of local force feedback (FF) loops in terms of improving the robustness of teleoperation system stability and performance. In the experiments in Section III, which are performed using a haptics-enabled master–slave testbed developed in our lab, we compare the performance of the two-channel (2CH) and the four-channel (4CH) bilateral control architectures during soft-tissue palpation tests and explore the role of local FF terms.

In a minimally invasive surgery, a force sensor on the surgical robot is required to be mounted on the section of the surgical instrument that goes past the port and inside the patient in order to avoid picking up friction and disturbance at the entry port. This requirement complicates the design of the robotic arm, creates sterilization issues, and raises the cost of the system. The bottom line is that in the current surgical systems (e.g., the

Manuscript received November 6, 2006; revised April 10, 2007. This work was supported by the Natural Sciences and Engineering Research Council of Canada under Grants RGPIN-1345 and RGPIN-227612, the Ontario Research and Development Challenge Fund under Grant 00-May-0709, and infrastructure grants from the Canada Foundation for Innovation awarded to the London Health Sciences Centre (CSTAR) and the University of Western Ontario. This paper was recommended by Associate Editor J. Q. Gan.

M. Tavakoli is with the School of Engineering and Applied Sciences, Harvard University, Cambridge, MA 02138 USA (e-mail: tavakoli@seas.harvard.edu).

A. Aziminejad and R. V. Patel are with the Department of Electrical and Computer Engineering, University of Western Ontario, London, ON N6A 5B9, Canada, and with Canadian Surgical Technologies and Advanced Robotics, London, ON N6A 5A5, Canada (e-mail: aazimin@uwo.ca; rajni@eng.uwo.ca).

M. Moallem is with the School of Engineering Science, Simon Fraser University, Burnaby, BC V5A 1S6, Canada (e-mail: mmoallem@sfu.ca).

Color versions of one or more of the figures in this paper are available online at http://ieeexplore.ieee.org.

Digital Object Identifier 10.1109/TSMCB.2007.903700

da Vinci system from Intuitive Surgical Inc., Sunnyvale, CA), due to limitations in the present actuator and sensor technology, there are only unilateral flows of the surgeon's hand motions and camera vision data from the master side to the slave side and vice versa with no haptic feedback. While there are efforts underway to add force sensors in surgical systems [6], [7], the study conducted in Sections II and III highlights what haptic feedback can add to teleoperation in terms of teleoperation fidelity.

Considering the other end of the spectrum, the second question that we address is as follows: if a haptic HMI is not available, can slave-side force measurement be of any help with regard to improving surgical outcomes? To answer this question, in Section IV, we discuss providing alternative modes of sensory feedback to the surgeon about instrument/tissue interaction, such as a graphical display of haptic information. Using our master–slave testbed, experiments that involve a lump localization task are conducted, and the performance of human subjects is compared for different modalities of instrument/tissue contact feedback.

The third question in this paper is the following. The currently available surgical systems provide visual feedback but no haptic feedback to the surgeon; yet, surgeons have relied on visual feedback for performing complicated interventions such as coronary artery bypass grafting [8]. Can haptic feedback offer any help specially if the visual feedback has a poor quality? For this question, in Section V, user performance is compared for a telemanipulated soft-tissue stiffness discrimination task when users are provided with visual feedback, haptic feedback, and graphical substitution for haptic feedback.

II. Stability and Transparency in Haptic Teleoperation

For safe and precise teleoperation, stability and transparency of the master–slave system are essential. As a performance measure, Lawrence [9] defined transparency as "the description of the degree of telepresence of the remote site available to the human operator through the teleoperator device." Transparency of a bilaterally controlled teleoperator depends on how well the slave/environment interaction forces are reflected to the user's hand by the master. Denoting the hand/master interaction as f_h and the slave/environment interaction as f_e, the dynamics of the master and the slave can be written as

$$f_m + f_h = M_m \ddot{x}_m \quad f_s - f_e = M_s \ddot{x}_s \tag{1}$$

where M_m, M_s, x_m, x_s, f_m, and f_s are the master and the slave inertias, positions, and control signals (force or torque), respectively. In an ideally transparent teleoperation system, through appropriate control signals f_m and f_s, the master and the slave positions and interactions will match regardless of the operator and environment dynamics, i.e.,

$$x_m = x_s \quad f_h = f_e. \tag{2}$$

By considering velocities and forces in a teleoperation system as currents and voltages, an equivalent circuit representation of the system can be obtained [10] (Fig. 1), in which impedances $Z_h(s)$ and $Z_e(s)$ denote dynamic characteristics of the human operator's hand and the remote environment, respectively. Here, F_h^* and F_e^* are the operator's and the environment's exogenous input forces, respectively, and are independent of the teleoperation system behavior. It is generally assumed that the environment is passive ($F_e^* = 0$), and the operator is passive in the sense that he/she does not perform actions that will make the teleoperation system unstable.

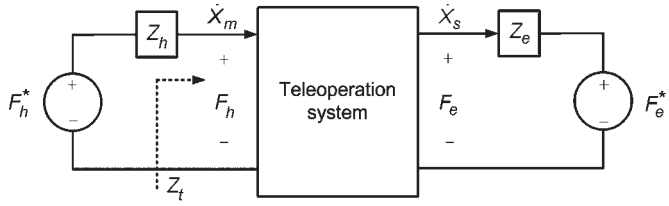

Fig. 1. Equivalent circuit representation of a teleoperation system.

To evaluate the transparency of teleoperation, the hybrid representation of the two-port network model of a master–slave system is most suitable. In this representation,

$$\begin{bmatrix} F_h \\ -\dot{X}_s \end{bmatrix} = \begin{bmatrix} h_{11} & h_{12} \\ h_{21} & h_{22} \end{bmatrix} \begin{bmatrix} \dot{X}_m \\ F_e \end{bmatrix}. \tag{3}$$

Note that throughout this paper, we have used velocities in dynamic representation rather than positions. This convention does not affect our analysis, although it might possibly cause small offsets between master and slave positions (steady-state errors in positions). As Lawrence [9] has mentioned, these position offsets can be compensated for through position indexing (usually utilized in a bilateral teleoperation to overcome workspace limitations of the master robot) and visual feedback. From (2) and (3), a perfect transparency is achieved if and only if the hybrid matrix has the following form:

$$H_{\text{ideal}} = \begin{bmatrix} 0 & 1 \\ -1 & 0 \end{bmatrix}. \tag{4}$$

Each element of the H matrix has a physical meaning. The hybrid parameter $h_{11} = F_h/\dot{X}_m|_{F_e=0}$ is the input impedance in free-motion condition. Nonzero values for h_{11} mean that even when the slave is in free space, the user will receive some FF, thus giving a "sticky" feel of free-motion movements. The parameter $h_{12} = F_h/F_e|_{\dot{X}_m=0}$ is a measure of force tracking for the haptic teleoperation system when the master is locked in motion (perfect force tracking for $h_{12} = 1$). The parameter $h_{21} = -\dot{X}_s/\dot{X}_m|_{F_e=0}$ is a measure of position (velocity) tracking performance when the slave is in free space (perfect position/velocity tracking for $h_{21} = -1$). The parameter $h_{22} = -\dot{X}_s/F_e|_{\dot{X}_m=0}$ is the output admittance when the master is locked in motion. Nonzero values for h_{22} indicate that even when the master is locked in place, the slave will move in response to slave/environment contacts.

For the analysis of stability of a teleoperation system, according to Fig. 1, the knowledge of the human operator and the environment dynamics are needed in addition to the teleoperation system model (3). However, assuming that $Z_h(s)$ and

$Z_e(s)$ are passive, we might be able to draw stability conditions that are independent of the human operator and the environment (*absolute stability*). The necessary and sufficient conditions for absolute stability [stability under all passive terminations $Z_h(s)$ and $Z_e(s)$] of a two-port network are given by the following theorem [11]:

Theorem 1 (Llewellyn's Criterion): The teleoperation system (3) is absolutely stable if and only if 1) $h_{11}(s)$ and $h_{22}(s)$ have no poles in the right half plane (RHP); 2) any poles of $h_{11}(s)$ and $h_{22}(s)$ on the imaginary axis are simple with real and positive residues; and 3) for $s = j\omega$ and all real values of ω

$$\Re(h_{11}) \geq 0 \tag{5}$$

$$\Re(h_{22}) \geq 0 \tag{6}$$

$$2\Re(h_{11})\Re(h_{22}) - \Re(h_{12}h_{21}) - |h_{12}h_{21}| \geq 0 \tag{7}$$

where $\Re(\cdot)$ and $|\cdot|$ denote the real and absolute values, respectively.

For achieving the ideal response (4), various teleoperation control architectures are proposed in the literature. These control architectures are usually classified as position–force (i.e., position control at the master side and force control at the slave side), force–position, position–position, and force–force architectures. Among these four architectures, in order to have a stiff slave, we are interested in those in which the slave is under position control, namely, position–position and force–position. A more general classification is by the number of communication channels that are required for transmitting position and force values from the master to the slave and vice versa in each bilateral control architecture. In the following, we discuss the stability and the transparency of the aforementioned 2CH architectures in addition to a more sophisticated 4CH architecture.

A. 2CH Architectures

1) Position Error Based (PEB): A position-error-based, also called position–position, teleoperation architecture is shown in Fig. 2(a). The impedances $Z_m(s) = M_m s$ and $Z_s(s) = M_s s$ represent the dynamic characteristics of the master robot and the slave robot, respectively. Also, $C_m = (k_{v_m} s + k_{p_m})/s$ and $C_s = (k_{v_s} s + k_{p_s})/s$ are proportional-derivative controllers that are used at the master and the slave, respectively (here, the master and the slave velocities are fed to the two controllers).

As can be seen in Fig. 2(a), the PEB controller does not use any force sensor measurements (no shaded block with a force input) and merely tries to minimize the difference between the master and the slave positions, thus reflecting a force proportional to this difference to the user once the slave makes contact with an object. The hybrid matrix for this architecture is given as

$$H = \begin{bmatrix} Z_m + C_m \frac{Z_s}{Z_{ts}} & \frac{C_m}{Z_{ts}} \\ -\frac{C_s}{Z_{ts}} & \frac{1}{Z_{ts}} \end{bmatrix} \tag{8}$$

where $Z_{tm} = Z_m + C_m$ and $Z_{ts} = Z_s + C_s$. As a result, in addition to nonideal force tracking $(h_{12} \neq 1)$, the PEB method suffers from a distorted perception in free-motion condition $(h_{11} \neq 0)$. This means that in the absence of a slave-side force sensor, control inaccuracies (i.e., nonzero position errors) lead to proportional FF to the user even when the slave is not in contact with the environment.

Theorem 2: The PEB teleoperation system of Fig. 2(a) is absolutely stable if $k_{v_m}, k_{p_m}, k_{v_s}, k_{p_s} > 0$ and $C_m(s)/C_s(s) = \alpha$, where α is a positive constant.

Proof: To investigate the stability of this system using Theorem 1, the characteristic polynomial for h_{11} and h_{22} is $M_s s^2 + k_{v_s} s + k_{p_s}$, which has no RHP poles if $k_{v_s}, k_{p_s} > 0$. With respect to conditions (5) and (6), we have

$$\Re(h_{11}) = \frac{M_s \left(k_{v_s} k_{p_m} - k_{v_m} k_{p_s} + M_s k_{v_m} \omega^2\right)}{k_{v_s}^2 + \left(-k_{p_s}/\omega + M_s \omega\right)^2} \tag{9}$$

$$\Re(h_{22}) = \frac{k_{v_s}}{k_{v_s}^2 + \left(-k_{p_s}/\omega + M_s \omega\right)^2} \tag{10}$$

which are nonnegative if $k_{v_m}, k_{v_s} > 0$ and

$$k_{v_s} k_{p_m} - k_{v_m} k_{p_s} = 0. \tag{11}$$

Also, the equality to zero in condition (7) holds if (11) holds and $k_{v_m}, k_{p_m} > 0$. ■

2) Direct Force Reflection (DFR): A DFR, also called force–position, teleoperation architecture is shown in Fig. 2(b). This method requires a force sensor to measure the interactions between the slave and the environment. The hybrid parameters for the force–position architecture are given as

$$H = \begin{bmatrix} Z_m & 1 \\ -\frac{C_s}{Z_{ts}} & \frac{1}{Z_{ts}} \end{bmatrix}. \tag{12}$$

Consequently, although the perception of free motion is still less than ideal $(h_{11} \neq 0)$, a perfect force tracking is attained $(h_{12} = 1)$. Nonetheless, compared to the PEB method, h_{11} is much closer to zero in the DFR method, and the user only feels the inertia of the master interface when the slave is not in contact. Although the DFR method proves to be better than the PEB method, both methods suffer from the less-than-ideal h_{21} and h_{22} values, which results in poor position tracking response and slave stiffness. In Section II-B, we will explain how a 4CH architecture can fulfill all of the conditions of the ideal response (4).

Theorem 3: The DFR teleoperation system of Fig. 2(b) is absolutely stable if $k_{v_s}, k_{p_s} > 0$ and $|C_s| \gg |Z_s|$.

Proof: To investigate the stability via Theorem 1, h_{11} has no poles, and the characteristic polynomial for h_{22} is $M_s s^2 + k_{v_s} s + k_{p_s}$, which has no RHP poles if $k_{v_s}, k_{p_s} > 0$. Also, $\Re(h_{11}) = 0$, and $\Re(h_{22})$ is same as (10), which is nonnegative if $k_{v_s} > 0$. Also, condition (7) is simplified to

$$\Re\left(\frac{C_s}{C_s + Z_s}\right) - \left|\frac{C_s}{C_s + Z_s}\right| \geq 0. \tag{13}$$

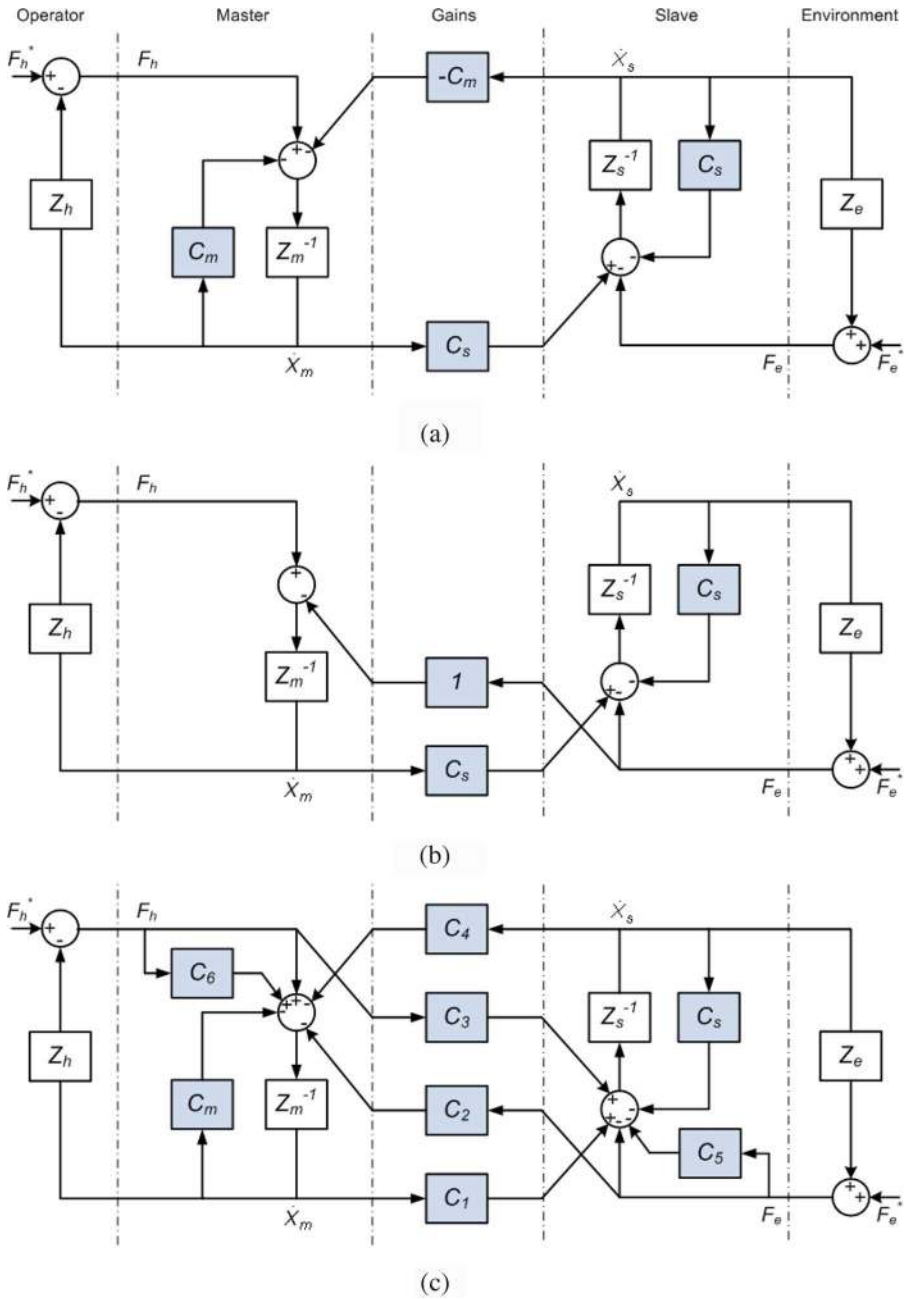

Fig. 2. (a) Position-error-based, (b) direct force reflection, and (c) 4CH bilateral control architectures. The shaded blocks represent control components.

Equation (13) holds if and only if

$$\Im\left(\frac{C_s}{C_s+Z_s}\right)=\frac{k_{v_s}\omega M_s}{k_{v_s}^2+\left(-k_{p_s}/\omega+M_s\omega\right)^2}=0 \qquad (14)$$

which is mathematically true provided that $k_{v_s}=0$, i.e., no derivative term is used at the slave side, which is not a viable option. However, the imaginary part (14) approaches zero if $k_{p_s}\to\infty$, $k_{v_s}\to\infty$, or $M_s\to 0$, which can be summarized as $|C_s|\gg|Z_s|$. ■

Using a loop-shaping filter can help to achieve a higher degree of absolute stability [12]. Nevertheless, the above discussion is conservative, as it ensures stability regardless of the teleoperation system's terminations. For a less conservative study, taking into account the remote environment impedance Z_e, i.e., $F_e=Z_e\dot{X}_s$, the general teleoperation system given by (3) has the following transfer function from F_h to $\dot{X}_m$:

$$\frac{\dot{X}_m}{F_h}=\frac{1+h_{22}Z_e}{h_{11}(1+h_{22}Z_e)-h_{12}h_{21}Z_e}. \qquad (15)$$

Assuming the environment is modeled by a linear spring, i.e., $Z_e=k_e/s$, the characteristic equation for the transfer function from F_h to $\dot{X}_m$ (and to any other output), which must have no zeros in the RHP for the teleoperation system to be stable, is given by

$$h_{11}s+k_e(h_{11}h_{22}-h_{12}h_{21})=0. \qquad (16)$$

Using the hybrid parameters (12) and $C_s = (k_{v_s}s + k_{p_s})/s$, (16) simplifies to $M_m M_s s^4 + M_m k_{v_s} s^3 + M_m(k_e + k_{p_s})s^2 + k_e k_{v_s} s + k_e k_{p_s} = 0$. Applying the Routh–Hurwitz criterion to this characteristic equation, the necessary and sufficient conditions for asymptotic stability of the teleoperation system are

$$\begin{aligned}\Delta_1 &= \frac{k_{v_s}}{M_s} > 0\\ \Delta_2 &= \frac{k_{v_s}\left[\beta k_{p_s} + k_e(\beta-1)\right]}{M_s M_m} > 0\\ \Delta_3 &= \frac{k_{v_s}^2 k_e^2(\beta-1)}{M_s^2 M_m^2} > 0\\ \Delta_4 &= \frac{k_{v_s}^2 k_e^3 k_{p_s}(\beta-1)}{M_s^3 M_m^3} > 0\end{aligned} \tag{17}$$

where $\beta = M_m/M_s$. The above condition set holds iff

$$k_{v_s} > 0 \quad k_{p_s} > 0 \quad \beta > 1. \tag{18}$$

Although we have considered a unity FF gain in Fig. 2(b), if a gain $k_f \neq 1$ is used, the condition $\beta > 1$ is changed to $\beta > k_f$. The condition set (18) guarantees stability independent of frequency.

B. 4CH Architecture

Fig. 2(c) depicts a general 4CH bilateral teleoperation architecture [9], [13]. This architecture can represent other teleoperation structures through the appropriate selection of subsystem dynamics C_1 to C_6. The compensators C_5 and C_6 in Fig. 2(c) constitute a local FF at the slave side and the master side, respectively. The h parameters for the 4CH architecture in Fig. 2(c) are

$$\begin{aligned}h_{11} &= (Z_{ts}Z_{tm} + C_1C_4)/D\\ h_{12} &= \left[Z_{ts}C_2 - (1+C_5)C_4\right]/D\\ h_{21} &= -\left[Z_{tm}C_3 + (1+C_6)C_1\right]/D\\ h_{22} &= -\left[C_2C_3 - (1+C_5)(1+C_6)\right]/D\end{aligned} \tag{19}$$

where $D = -C_3C_4 + Z_{ts}(1+C_6)$.

In contrast to the 2CH architectures, a sufficient number of parameters [degrees of freedom (DOFs)] in the 4CH architecture enable it to achieve ideal transparency. In fact, by selecting C_1 through C_6 according to

$$C_1 = Z_{ts} \quad C_2 = 1 + C_6 \quad C_3 = 1 + C_5 \quad C_4 = -Z_{tm} \tag{20}$$

the ideal transparency conditions (4) are fully met.

For the analysis of stability, we need to use the scattering theory, which is a powerful tool for investigation of absolute stability in two-port networks. Fig. 3 depicts a scattering matrix representation of a bilateral teleoperation system and is expressed by $b = S(s)a$. Here, $a = [a_1\ a_2]^T$ and $b = [b_1\ b_2]^T$ are the input and output waves of the teleoperation system, respectively, and are related to equivalent voltages and currents as

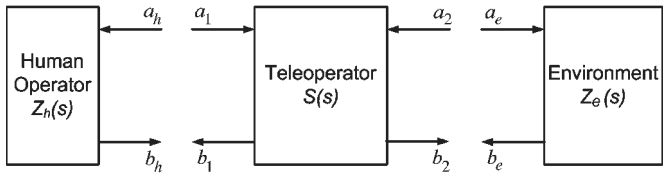

Fig. 3. Generalized description of a bilateral teleoperation system in terms of scattering parameters.

$a = (F + n^2\dot{X})/2$ and $b = (F - n^2\dot{X})/2$, where $F = [F_h\ F_e]^T$, $\dot{X} = [\dot{X}_m\ -\dot{X}_s]^T$, and n is a scaling factor.

Theorem 4: The necessary and sufficient condition for the stability in a reciprocal two-port network ($S_{12} = S_{21}$) with an RHP-analytic scattering matrix $S(s)$ that is terminated with a passive operator and a passive environment is [14]

$$\bar{\sigma}\left[S(j\omega)\right] \leq 1 \tag{21}$$

where $\bar{\sigma}$ represents the maximum singular value of $S(j\omega)$. In the case of a nonreciprocal two-port network, the passivity condition (21) is only a sufficient condition for stability.

Theorem 5: The necessary and sufficient condition for the absolute stability of the 4CH teleoperation system of Fig. 2(c) under ideal transparency conditions is that all coefficients of polynomial

$$\begin{aligned}D &= C_3Z_{tm} + C_2Z_{ts}\\ &= (M_mC_3 + M_sC_2)s^2 + (k_{dm}C_3 + k_{ds}C_2)s\\ &\quad + k_{pm}C_3 + k_{ps}C_2\end{aligned} \tag{22}$$

have the same sign.

Proof: In the 4CH architecture, when the ideal transparency condition set (20) holds, the hybrid matrix is

$$H = \begin{bmatrix} 0 & \frac{D}{D} \\ -\frac{D}{D} & 0 \end{bmatrix} \tag{23}$$

where D is found to be as given in (22) given that $Z_{tm} = M_m s + C_m(s) = M_m s + k_{dm} + k_{pm}/s$ and $Z_{ts} = M_s s + C_s(s) = M_s s + k_{ds} + k_{ps}/s$. The above hybrid matrix corresponds to the following scattering matrix:

$$S = \begin{bmatrix} \frac{-D^2+D^2}{2D^2} & \frac{2D^2}{2D^2} \\ \frac{2D^2}{2D^2} & \frac{D^2-D^2}{2D^2} \end{bmatrix}. \tag{24}$$

For the scattering matrix S in (24) to be RHP analytic, D has to be Hurwitz. The necessary and sufficient condition for D being Hurwitz is that all the coefficients have the same sign. In this case, S can be simplified to

$$S = \begin{bmatrix} 0 & 1 \\ 1 & 0 \end{bmatrix}. \tag{25}$$

Both of the singular values of this matrix are equal to 1. Therefore, since, under ideal transparency condition, the system is reciprocal, according to (21), the system is absolutely stable iff all the coefficients in the polynomial D given in (22) have the same sign. ■

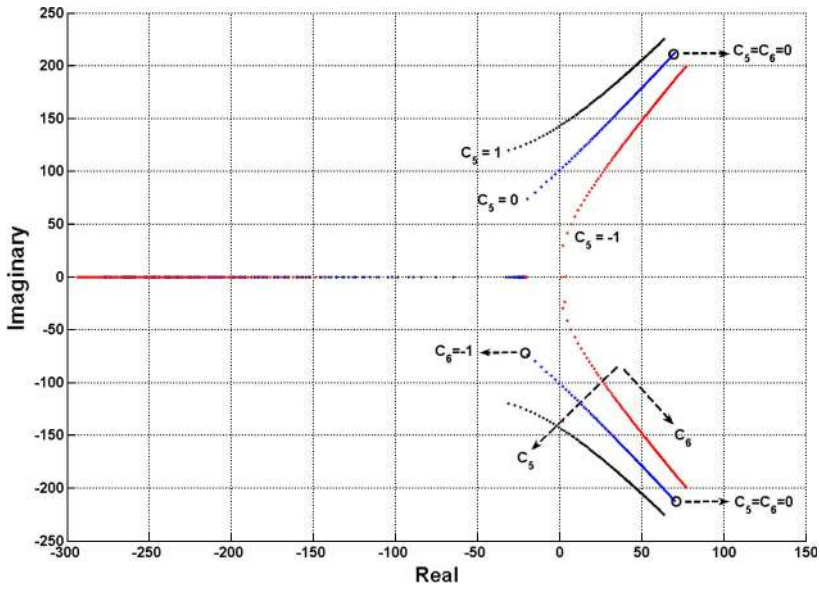

Fig. 4. Root loci of the poles of the 4CH teleoperation system with $\gamma = -1$ when $-1 \leq C_6 \leq 0$ and $C_5 = 1, 0, -1$.

1) Stability and Performance Robustness: It should be noted that under ideal transparent conditions, i.e., when the singular values of $S(s)$ are 1, the passivity (and stability) critically depends on the exact implementation of control laws and having the exact dynamics of the master and the slave, as any nonideality might increase the maximum singular value beyond unity. Such a low stability margin can be explained by the tradeoff that exists between stability and transparency in a bilateral teleoperation [9], [15]. In the following, we study the effects of two control implementation issues on the teleoperation system stability and performance.

In practice, the ideal transparency conditions $C_1 = Z_{ts} = C_s + Z_s$ and $C_4 = -Z_{tm} = -C_m - Z_m$ are difficult to exactly meet due to the noise that would be introduced into the system by the acceleration terms. Therefore, approximations $C_1 = C_s + (\gamma + 1)Z_s$ and $C_4 = -C_m - (\gamma + 1)Z_m$, where $-1 \leq \gamma < 0$, are made, which affect the teleoperation transparency and, more importantly, the stability of an already critically stable system. To examine the effect of $\gamma \neq 0$ on system stability, let us derive the characteristic polynomial for the transfer function $\dot{X}_m/F_h$, i.e.,

$$\begin{aligned} &M_m M_s(\gamma+2)\gamma s^4 + (M_m k_{v_s} + M_s k_{v_m})\,\gamma s^3 \\ &\quad + (M_s k_{p_m} + M_m k_{p_s} - k_e M_s(1+C_6))\,\gamma \\ &\quad - (k_e M_m(1+C_5) + k_e M_s(1+C_6))\,s^2 \\ &\quad - (k_e k_{v_m}(1+C_5) + k_e k_{v_s}(1+C_6))\,s \\ &\quad - (k_e k_{p_m}(1+C_5) + k_e k_{p_s}(1+C_6)) = 0. \end{aligned} \tag{26}$$

Fortunately, when $\gamma \neq 0$, the presence of the local FF terms C_5 and C_6 gives extra DOFs to stabilize an otherwise unstable system. To further illustrate this point, consider $M_m = 5.968 \times 10^{-4}$ kg $\cdot$ m^2 and $M_s = 9.814 \times 10^{-3}$ kg $\cdot$ m^2. These values have been extracted from our experimental setup, which will be described in Section III-A. Also, $C_m(s) = M_m(80s + 1600)/s$ and $C_m(s) = M_s(80s + 1600)/s$, which position the master and the slave closed-loop poles (in free motion) at $(-40, -40)$. Moreover, assume that the environment is modeled by a spring $Z_e = k_e/s$, where $k_e = 100$ N/m. If acceleration terms are ignored in the control laws C_1 and C_4 (i.e., $\gamma = -1$), the absence of the local FF terms ($C_5 = C_6 = 0$) leads to a pair of RHP poles (-280.3, -20.3, $70.3 \pm j212.2$). However, as shown in Fig. 4, introducing the local FF terms, e.g., $C_5 > -1$ and $C_6 = -1$, can shift the unstable poles to stable locations.

In order to investigate the effect of local FF on transparency when $\gamma \neq 0$, let us define the transparency transfer function of the general teleoperation system described by (3) as

$$T = \frac{Z_t}{Z_e} = \frac{h_{11} + (h_{11}h_{22} - h_{12}h_{21})Z_e}{(1 + h_{22}Z_e)Z_e} \tag{27}$$

where, as shown in Fig. 1, Z_t is the impedance that is transmitted to and felt by the operator. Under ideal transparency and $\gamma = 0$, we have $T = 1$ regardless of the remote environment Z_e. However, $\gamma \neq 0$ makes T dependent on Z_e. To reduce the dependence of T on Z_e, let us define the transparency sensitivity function as

$$S_T = \frac{\partial T}{\partial Z_e} = \frac{\gamma\,[Z_m(C_s + \gamma Z_s) + Z_m(C_m + 2Z_m)]}{[(1+C_5)(Z_{tm} + \gamma Z_m) + (1+C_6)Z_{ts}]\,Z_e^2}. \tag{28}$$

To see the effect of C_5 and C_6 on performance robustness, a sensitivity ratio is defined as

$$\begin{aligned} R &= \frac{S_T|_{C_5 \neq 0, C_6 \neq 0}}{S_T|_{C_5 = C_6 = 0}} \\ &= \frac{Z_m\gamma + Z_{tm} + Z_{ts}}{(1+C_5)(Z_{tm} + \gamma Z_m) + (1+C_6)Z_{ts}}. \end{aligned} \tag{29}$$

As it can be seen, compared to the case of no local FF, the presence of local FF terms, e.g., $C_6 = -1$ and sufficiently large

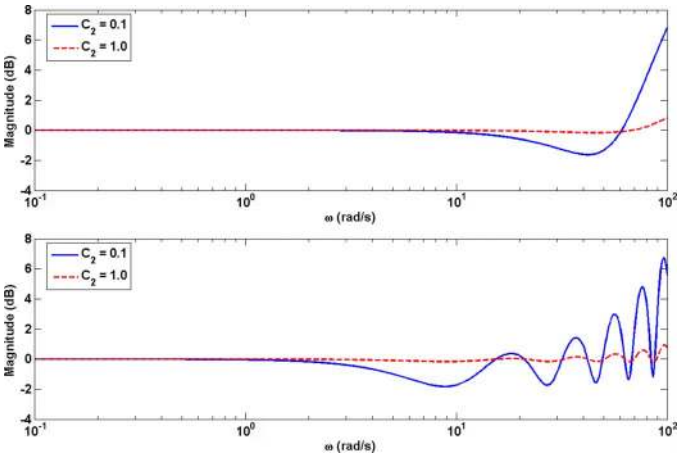

Fig. 5. Transparency transfer function magnitude for one-way delays (top) $T_d = 15$ ms and (bottom) $T_d = 150$ ms.

$C_5 > 0$, can make $R < 1$, thus reducing the dependence of the transparency transfer function T on Z_e.

Local FF terms C_5 and C_6 also help mitigate the undesirable effects of processing delay and communication latency between the master and the slave. In the presence of time delay T_d, in an ideally transparent bilateral teleoperation system

$$H = \begin{bmatrix} 0 & e^{-sT_d} \\ -e^{-sT_d} & 0 \end{bmatrix} \quad S = \begin{bmatrix} -\tanh(sT_d) & \operatorname{sech}(sT_d) \\ \operatorname{sech}(sT_d) & \tanh(sT_d) \end{bmatrix}. \tag{30}$$

It can be shown that $\bar{\sigma}(S)$ for this scattering matrix is unbounded; consequently, this system cannot maintain stability for all passive operators and environments. However, when Z_h and Z_e are factored in the analysis, the teleoperation system loses its reciprocity property, and therefore, although not passive, it can be stabilized by proper choices of Z_h and Z_e [16].

According to (27), the hybrid matrix (30) corresponds to the following ideal transparency transfer function: $T = e^{-2sT_d}$. In the 4CH architecture under time delay, when the ideal transparency condition set (20) holds, the transparency transfer function is given by

$$T = \frac{Z_{tm}C_3 + Z_{ts}C_2e^{-2sT_d} + Z_{tm}Z_{ts}/Z_e(1 - e^{-2sT_d})}{Z_e(1 - e^{-2sT_d})C_3C_2 + Z_{ts}C_2 + Z_{tm}e^{-2sT_d}C_3}. \tag{31}$$

It can easily be seen that in the absence of local FF terms $(C_6 = C_2 - 1 = 0, C_5 = C_3 - 1 = 0)$, $T \neq e^{-2sT_d}$. However, with nonzero C_5 and C_6, near-ideal transparency can be achieved. For instance, taking $C_5 = -1$, (31) will be reduced to $T = e^{-2sT_d} + (Z_{tm}/Z_eC_2)(1 - e^{-2sT_d})$, which approaches the ideal $T = e^{-2sT_d}$ by selecting a sufficiently large C_2. To further illustrate this point, Fig. 5 shows the magnitude of the frequency response of the transparency transfer function T for the example described earlier with $C_5 = -1$ and one-way delays of $T_d = 15$ ms (top) and $T_d = 150$ ms (bottom). Evidently, with an increase in C_2, the magnitude of T nears 1 over a relatively wide frequency range.

2) Three-Channel (3CH) Case: Another potential benefit of the general 4CH architecture of Fig. 2(c) is that by proper adjustment of the local feedback parameters, it is possible to obtain two classes of 3CH control architectures, which can be transparent under ideal conditions [16], [17]. The first class of 3CH architectures is derived by setting $C_2 = 1$ and $C_3 = 0$. As a consequence, $C_5 = -1$ and $C_6 = 0$. In other words, there is no need for master/operator interaction force measurement, and therefore, the number of sensors in the system can be reduced. The second class of 3CH architectures is obtained by setting $C_2 = 0$ and $C_3 = 1$. In this class, force measurement at the slave side is not needed. The need for fewer sensors without imposing additional expense on system transparency makes the 3CH architectures extremely attractive from the implementation point of view.

III. Haptic Teleoperation Experiments

A. Experimental Setup

For the experimental evaluation of the different haptic teleoperation control methods described in Section II, we used a bilateral master–slave system that was developed for endoscopic surgery experiments. Through a user interface (master), the user controls the motion of a surgical tool (slave) and receives force/torque feedback of the slave/tissue interactions. The developed master user interface is capable of providing the user with FF in all five DOFs available in endoscopic surgery (pitch, yaw, roll, insertion, and handle open/close) [18]. The developed slave endoscopic instrument is also capable of measuring interactions with tissue in all the five present DOFs [6]. In the experiments in this paper, the master and slave subsystems were constrained for force-reflective teleoperation in the twist direction only (i.e., rotations about the instrument axis). The digital control loop is implemented at a sampling frequency of 1000 Hz. As discussed in Appendix A, the friction and gravity effects that are present in the master were determined and compensated for such that the user does not feel any weight on his/her hand when the slave is not in contact with an object. Appendix A also includes the master system modeling and identification, whereby the friction-compensated master is represented as $\tau_m = M_m\ddot{\theta}_m$, where $M_m = 5.97 \times 10^{-4}$ kg $\cdot$ m^2. Using a similar method, the slave's model was identified as $\tau_s = M_s\ddot{\theta}_s$, where $M_s = 9.8 \times 10^{-3}$ kg $\cdot$ m^2.

B. Observation of Hand Forces

The 4CH bilateral control method requires the measurements of hand/master interactions f_h and slave/environment interactions f_e. In our master–slave system, whereas the slave's end-effector is sensorized to directly measure f_e, we need to use the dynamic model of the master to estimate f_h using a state observer. For this purpose, let us write the master dynamics $f_m + f_h = M_m\ddot{x}_m$ in state-space form by choosing $x_1 = x_m$ and $x_2 = \dot{x}_m$, i.e.,

$$\dot{x}_1 = x_2$$
$$\dot{x}_2 = {M_m}^{-1}(f_m + f_h).$$

To estimate the hand force f_h (and the joint velocity $\dot{x}_m$), the Nicosia observer was used [19], i.e.,

$$\begin{aligned}\dot{\hat{x}}_1 &= \hat{x}_2 + k_2 e \\ \dot{\hat{x}}_2 &= {M_m}^{-1}(x_m + k_1 e) \\ e &= x_1 - \hat{x}_1 \end{aligned} \tag{32}$$

where k_1 and k_2 are positive constants. The observer uses the joint position and the portion of the joint torque that comes from the controller to find the externally applied joint torque. It can be shown that the observer is asymptotically stable, and the error equation is

$$M_m \ddot{e} + k_2 M_m \dot{e} + k_1 e = f_h. \tag{33}$$

In steady state, $\ddot{e} = \dot{e} = 0$. Therefore, the hand force is estimated at low frequencies as $\overline{f}_h = k_1 e$.

C. Observer and Controller Gains

Using the dynamic model of the master (Appendix A) and in the absence of a force sensor at the master, the observer (32) was used to estimate the hand forces f_h. Using the observer's error dynamics (33), the gains k_1 and $k_2 = 2\sqrt{k_1/M_m}$ were chosen such that the observer has very fast critically damped poles at $(-350, -350)$.

For asymptotic convergence of the position and force errors in the 4CH architecture, the two controllers C_m and C_s should be chosen as [17]

$$\frac{C_s}{C_m} = \frac{M_s}{M_m}. \tag{34}$$

Therefore, we take $C_m = M_m(k_v s + k_p)/s$ and $C_s = M_s(k_v s + k_p)/s$, noting that the master and the slave velocities are fed to the two controllers. To place the master and the slave closed-loop poles for fast responses, $(k_p\ k_v) = (1600\ \ 80)$ were chosen. This results in the position error characteristic equation $\ddot{e}_x + 80\ \dot{e}_x + 1600\ e_x = 0$, where $e_x = x_m - x_s$, for both the master and the slave (both in free space), thus moving the closed-loop poles of the master and the slave to $(-40, -40)$.

D. Soft-Tissue Palpation Tests

In a palpation test, the user twists the master back and forth, which causes the slave to repeatedly probe a soft tissue using a small rigid beam that is attached to the slave's end-effector for 60 s. The user receives haptic feedback of instrument/tissue interactions in real time. In addition to the aforementioned tests and to further investigate the relative transparency of systems, a second set of free-motion tests are performed, which, in conjunction with the previous contact-mode tests, can be used to determine the hybrid parameters of the teleoperation system in the frequency domain. In the free-motion tests, the master is moved back and forth by the user for about 60 s, whereas the slave's tip is in free space. Since $f_e = 0$, the frequency responses $h_{11} = F_h/X_m$ and $h_{21} = -X_s/X_m$ can be found

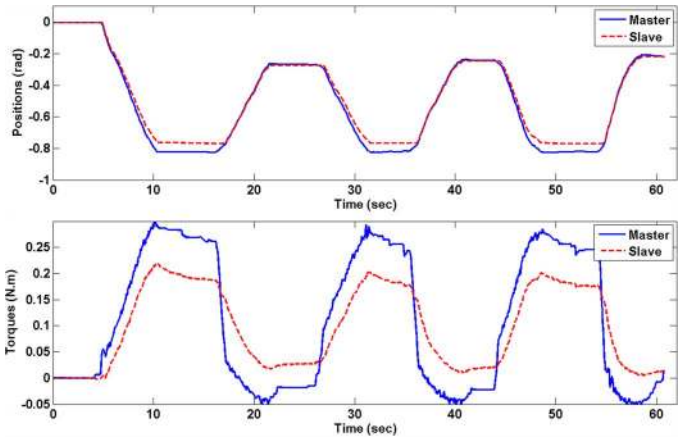

Fig. 6. Position and force profiles for the PEB teleoperation system.

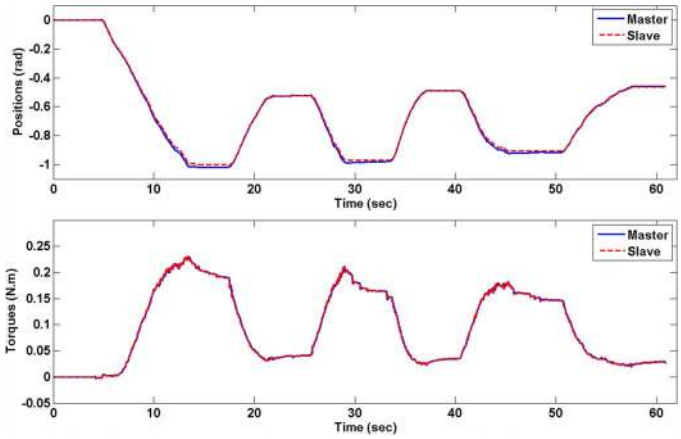

Fig. 7. Position and force profiles for the DFR teleoperation system.

by applying spectral analysis (MATLAB function *spa*) on the free-motion test data (for the two-port hybrid model based on positions rather than velocities). By using the contact-mode test data, the other two hybrid parameters can be obtained as $h_{12} = F_h/F_e - h_{11}X_m/F_e$ and $h_{22} = -X_s/F_e - h_{21}X_m/F_e$.

Fig. 6 shows the master and the slave positions and torque tracking profiles in the contact mode for the PEB teleoperation system. Fig. 7 illustrates the same profiles for the DFR system. The fact that the position profiles do not change sign is because during the palpation tests, the slave never breaks contact with the soft tissue. As can be seen, the DFR system displays a superior force tracking performance compared to PEB. The magnitudes of the hybrid parameters of the PEB and DFR teleoperation systems are shown in Fig. 8. Due to the human operator's limited input bandwidth, these identified hybrid parameters can be considered valid up to a frequency of 60 rad/s. Fig. 8 is an indication of the DFR's superiority in terms of transparent performance considering the ideal transparency requirement (4). As expected from (8) and (12), relatively high values of h_{11} for PEB are evidence of the fact that even when the slave is in free space, the user will feel some force, which gives a "sticky" feel of free-motion movements. On the other hand, since DFR uses f_e measurements, its input impedance in free-motion condition (h_{11}) will be lower, which makes the feeling of free space much more realistic. The better force

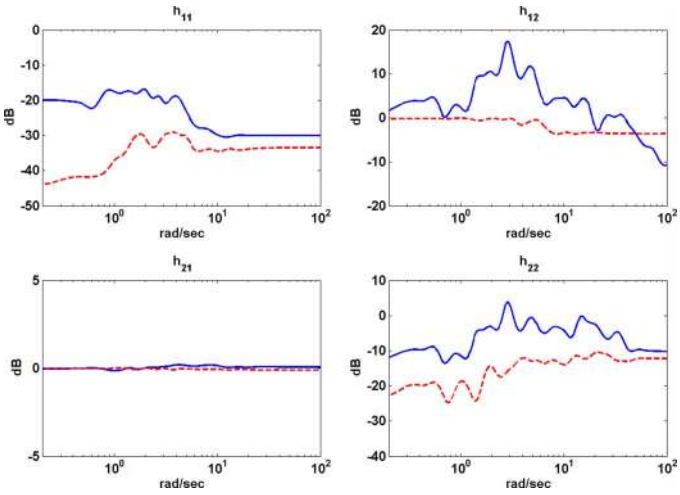

Fig. 8. Magnitudes of the hybrid parameters for the 2CH teleoperation systems. (Solid) PEB. (Dashed) DFR.

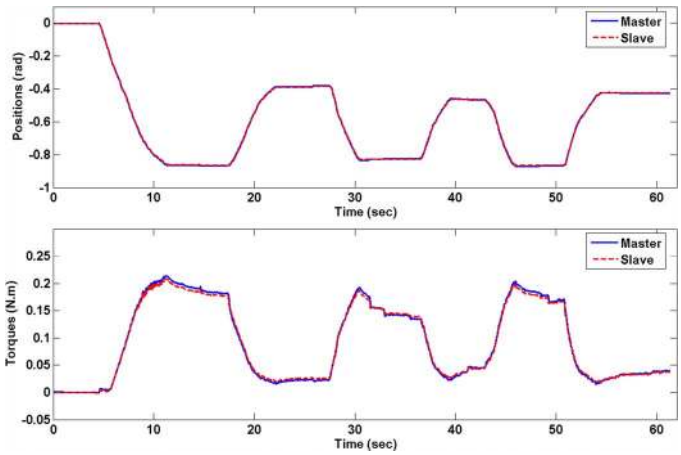

Fig. 9. Position and force profiles for the 3CH teleoperation system with $C_3 = 0$ and $C_5 = -1$.

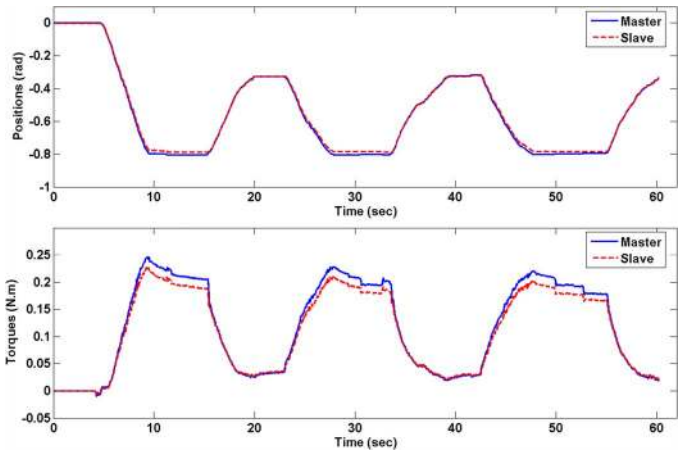

Fig. 10. Position and force profiles for the 4CH teleoperation system with $C_3 = 0.5$ and $C_5 = -0.5$ (4CH-1).

tracking performance of DFR, i.e., $h_{12} \approx 0$ dB, agrees with the time-domain plots of Figs. 6 and 7 and, confirms (12). With regard to h_{21}, both spectra are close to 0 dB, which indicates that both systems ensure good position tracking in free space. These results are in accordance with (8) and (12). However, as can be seen from Figs. 6 and 7, contact-mode position tracking is better with DFR. With regard to h_{22}, it is important to note that because of the finite stiffness of the slave and also the backlash present in the slave's gearhead, the accuracy of $h_{22} = -X_s/F_e|_{X_m=0}$ estimates is less than that of the rest of the hybrid parameters.

As was discussed earlier, in practical implementation of the 4CH architecture, we do not consider the acceleration terms in the controllers C_1 and C_4 given in (20) as a noise reduction measure. Moreover, we limit our experimental study to the case where $C_6 = 0$. The reason for this is that, as reported in [16], the master local FF ($C_6 \neq 0$) is suitable for operations in which the environment is heavier, has more damping, and is stiffer than the operator's arm such as in remote excavation (as opposed to soft-tissue applications).

Fig. 9 shows the master and the slave positions and torque tracking profiles for the 3CH teleoperation system in which $C_2 = 1$, $C_6 = 0$, $C_3 = 0$, and $C_5 = -1$. Figs. 10 and 11 show similar profiles for the same choice of C_2 and C_6 but for $C_3 = 0.5$, $C_5 = -0.5$ (4CH system no. 1), and $C_3 = 1$, $C_5 = 0$ (4CH system no. 2), respectively. As can be seen, as the local FF gain at the slave is reduced (i.e., lower $|C_5|$), the contact-mode position tracking and, more significantly, the force tracking performance deteriorate. This can partially be attributed to the fact that when the slave local FF is reduced, there is an increased level of contribution of the observed force in the slave control action ($C_3 f_h$), which pronounces observation errors. Figs. 9–11 show that the 3CH architecture (with $C_3 = 0$) can lead to at least an equal level of performance compared to the 4CH architecture, although it needs one force sensor less. The 3CH architecture is also superior in the sense that, generally, a higher gain of the slave local feedback (i.e., higher $|C_5|$) allows for a lower gain of the master force feedforward (i.e., lower C_3) and, consequently, higher stability margin at no extra penalty on transparency. The magnitudes of the hybrid parameters of the 3CH and the two 4CH teleoperation systems are shown in Fig. 12. As can be seen, the magnitude of h_{12} over low frequencies, which is indicative of steady-state force tracking error, increases above 0 dB, as the gain of slave local FF is reduced. The slave local FF does not affect free-space position tracking as seen in the h_{21} spectra of Fig. 12.

Although, based on Figs. 7 and 9, it seems that the DFR architecture can offer performance comparable to the 3CH architecture, it must be noted that the above experiments have been performed using a soft object made of a silicon-based tissue phantom from Chamberlain Group (http://www.thecgroup.com), which is placed on top of a layer of foam. Under hard contact (using a piece of wood instead of the tissue phantom), however, the DFR shows degraded performance particularly in terms of position tracking [Fig. 13(a)], whereas the 3CH continues to satisfactorily perform in terms of both position tracking [Fig. 13(b)] and force tracking (not shown). Due to its optimum performance and relative simplicity of implementation, the 3CH architecture is used for haptic teleoperation experiments in the rest of this paper.

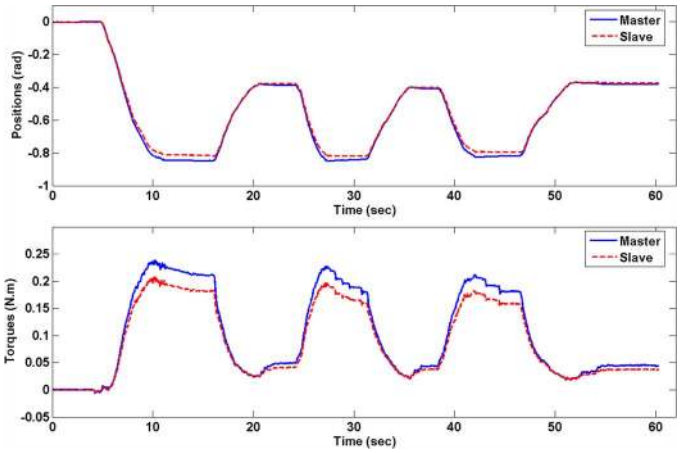

Fig. 11. Position and force profiles for the 4CH teleoperation system with $C_3 = 1$ and $C_5 = 0$ (4CH-2).

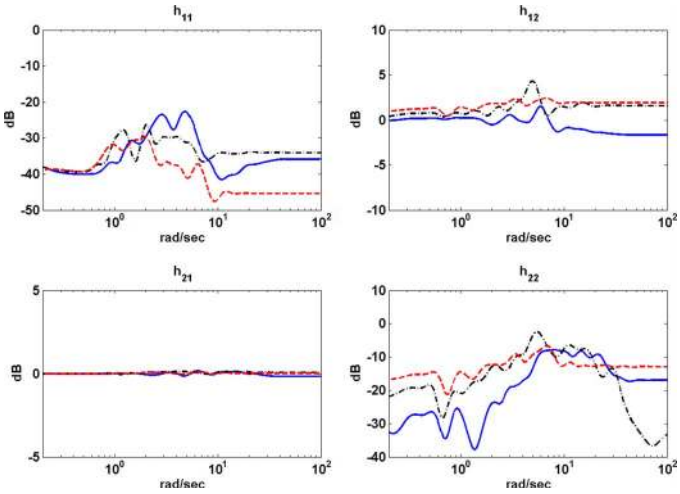

Fig. 12. Magnitudes of the hybrid parameters for 4CH teleoperation systems. (Solid) 3CH. (Dashed–dotted) 4CH-1. (Dashed) 4CH-2.

IV. Sensory Substitution for Haptic Feedback

As discussed in Section I, the lack of haptic feedback in the current surgical systems can cause complications and is a safety concern. As a solution to the problems that are caused by lack of haptic feedback, it is hypothesized that alternative modes of sensory feedback about instrument/tissue contacts can provide sufficient feedback of an instrument's contact with tissue and can improve surgical outcomes.

Depending on the nature of task, haptic feedback can be substituted in more than one way, e.g., by auditory, graphical, or vibrotactile cues. The graphical display of haptic information, i.e., "graphical FF" (GFF), as overlaid on or beside the endoscope view, can relay haptic information to the surgeon simply based on the size and/or the color of the visual stimuli.

In teleoperation applications with large time delays such as ground-to-space teleoperation, where it is difficult to compensate for the adverse effect of the large delay on haptic teleoperation system stability and performance, graphical substitution for haptic feedback is a viable alternative. Moreover, if the user interface has force reflection capability in fewer DOFs

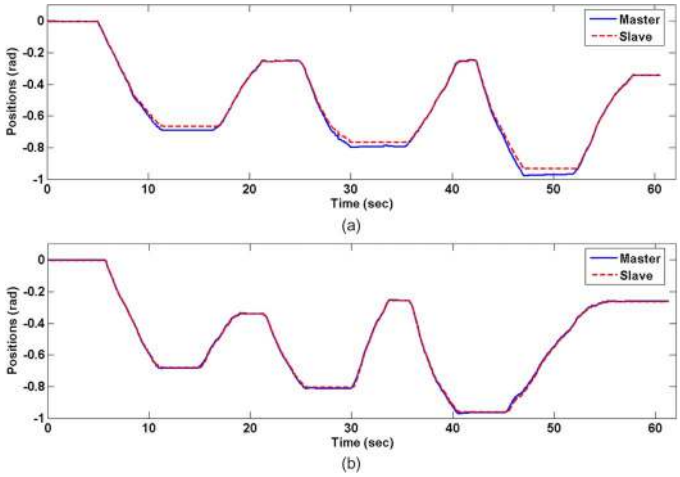

Fig. 13. Position profiles for (a) DFR and (b) 3CH teleoperation systems under hard contact.

than those of the task, a partial force reflection may destabilize the teleoperation system [20], in which case replacing haptic feedback by graphical feedback is useful. Graphical sensory substitution has been found to improve a user's sensitivity for detecting small forces by allowing the use of high feedback gains without slowing down hand movements [21]. For manual and telerobotics operations of a surgical knot-tying task, the forces applied in the robotic mode were closer to the forces applied in the manual mode when the users were provided with the auditory/graphical representation of the haptic information [22]. It would be interesting to see the difference between the haptic feedback and the graphical haptic feedback in the robotic mode itself. In the following, the two contact feedback modalities are compared in terms of their capability in transmitting critical task-related information to the user.

A. Case Study: Lump Localization Task

1) Experiment Design: Six subjects (two males and four females) aged 24–34 participated in our experiments. The subjects were engineering students with little to average exposure to haptic feedback and graphical substitution for haptic feedback. The task was to locate a rigid lump, which was embedded in an unknown location in a finite-stiffness homogeneous tissue model that was made from rubber. Lump localization was based on exploring the model and receiving haptic or graphical feedback using the master–slave setup (Fig. 14). The graphical cues about the levels of tool/tissue interaction forces were generated by an array of 16 light-emitting diodes that form a bar indicator for the magnitudes of forces. The lump was placed in one of five locations at approximately 34°, 65°, 92°, 124°, and 158° with respect to the horizon. The size of the lump (5 mm) was chosen such that users could detect the lump in a reasonable amount of time. Each lump localization trial started from orienting the master handle (and the slave's end-effector) such that it was horizontal, followed by twisting the handle to explore the tissue until the handle was again horizontal on the other side (equal to a wrist rotation of $+180^\circ$ for the user).

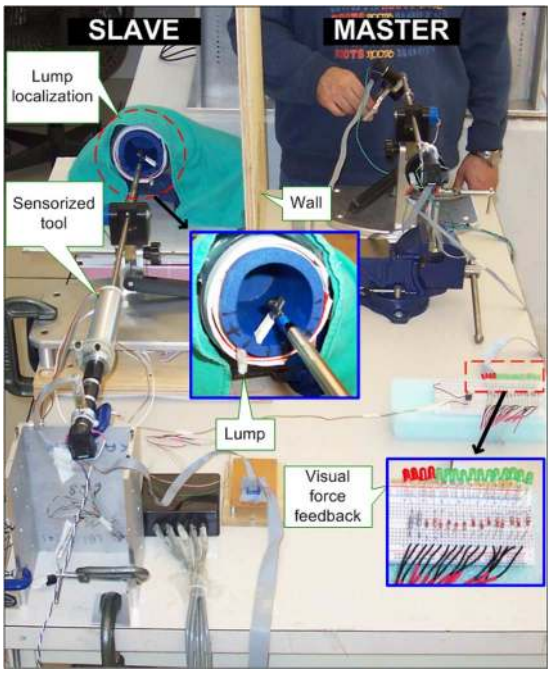

Fig. 14. Master–slave setup for performing telemanipulated lump localization.

The subjects' primary goal was defined as pinpointing the lump by centering the slave end-effector on it. The subjects were told that the task completion time was a secondary performance metric that needed to be minimized; yet, they could take their time if it helped to minimize the primary performance metric (i.e., localization error). This is different from most of the previous studies on sensory substitution, which have considered task completion time as the only metric for performance comparisons. A task was considered complete upon the subject's verbal signal that the lump was found.

Each subject performed two sets of tests with a short break between them. In each test, each of the five lump locations was presented twice to the subject: once in the presence of GFF about the levels of instrument/tissue interaction, and once in the presence of FF. For a fair comparison between FF and GFF, the two feedback modalities were presented with almost the same sensitivity (resolution) to the human subjects. Therefore, in each test, there were ten trials (i.e., ten combinations of lump location and feedback mode). The trials within a test were presented in a randomized order to the subjects. Before the experiments, each subject was given three to four practice trials until he or she felt comfortable with the operation of the master–slave system.

The subjects did not have camera vision from the slave side in order to keep tissue deformation cues from playing a role in lump localization—we do not consider nodules that can be visually detected through moving a tissue. Also, to mask any audio feedback that can result from the friction between the tissue model and the slave's end-effector, the subjects wore headphones that played music loud enough to mask out any external sounds.

In each trial of each test, the instrument/tissue contact forces, the end-effector position, and the task completion time were recorded. In addition to localization accuracy and task times, we also compared the energy supplied to tissue, as lower energy corresponds to less trauma and probably less tissue damage.

2) Results: As shown in Fig. 15(a), there is a consistency between the two feedback modalities in terms of the detected position of each lump. In order to compare the position errors, we used a two-tailed t-test and obtained the probability of the null hypothesis $\mu_1 = \mu_2$ for the five lump locations. The probability of the results assuming the null hypothesis for lump locations 1 to 5 were $p = 0.00019$, $p = 0.028$, $p = 0.515$, $p = 0.413$, and $p = 0.714$, respectively. These results indicate that for lump locations 3, 4, and 5, there is no significant difference in mean localization error between GFF and FF. This might be partly due to the fact that the subjects experienced some difficulty in localizing the first two lump positions, as they were too close to the starting point of the slave. In order to further investigate the accuracy of lump localization, we performed a one-way analysis of variance [(ANOVA) Appendix B] test on the localization error statistics of the five lump locations for both GFF and FF ($F(4, 82) = 0.4589$, $p = 0.766$ for GFF; and $F(4, 82) = 3.31$, $p = 0.014$ for FF). These results indicate that the localization error means do not significantly vary across the five lump locations for GFF but do significantly vary for FF.

Fig. 15(b) depicts the statistics of the time (in seconds) taken to localize a lump in each of the five locations. As a general observation, the mean localization time is significantly longer with GFF than with FF (267%, 192%, 201%, 151%, and 195% longer for lump locations 1 to 5, respectively). Right-tailed t-tests between GFF and FF for localization times of each lump location confirm this observation ($p = 4.515 \times 10^{-5}$, $p = 0.0013$, $p = 0.00017$, $p = 0.00036$, and $p = 0.00011$ for lump locations 1 to 5, respectively). In order to investigate the effect of lump positions on the exploration time, a one-way ANOVA test was conducted on the exploration time statistics of the five lump locations for both GFF and FF ($F(4, 82) = 1.119$, $p = 0.353$ for GFF; and $F(4, 82) = 2.579$, $p = 0.043$ for FF). These results confirm the fact that the exploration time means do not significantly vary across the five lump locations for GFF but significantly vary for FF.

Fig. 15(c) depicts the statistics of the energy [in joules; calculated as $\int_0^T f(t)v(t)dt$, where T, f, and v are the task completion time, the contact force, and the slave's velocity, respectively] that is supplied to the tissue during lump localization for each of the five lump locations with GFF and with FF. Excluding the first location, FF-based lump localization seems to supply more energy to the tissue in comparison to GFF. Again, we tested this hypothesis by means of a right-tailed t-test ($p = 0.006$, $p = 0.141$, $p = 0.204$, $p = 0.001$, and $p = 0.003$ for lump locations 1 to 5, respectively). These results show that the mean of the energy supplied to tissue under GFF and FF significantly varies for lump locations 1, 4, and 5. A one-way ANOVA test for the energy over the five lump locations yielded $F(4, 82) = 2.96$, $p = 0.0244$ for GFF and $F(4, 82) = 2.812$, $p = 0.0306$ for FF, which indicate significant variations across the five lump locations for both modalities.

3) Discussion: The following trends were observed in lump localization performance with GFF and with FF.

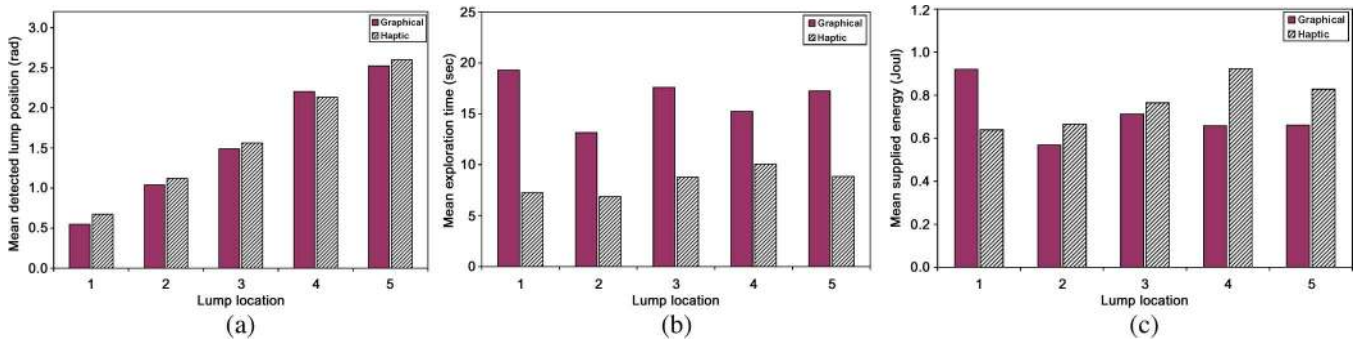

Fig. 15. (a) Mean detected lump position (in radians). (b) Mean exploration time (in seconds). (c) Mean energy supplied to the tissue (in joules).

The subjects were 100% successful in localizing the lumps under both GFF and FF with position errors significantly less than half the average distance between the lumps. No consistent trend was observed in favor of either approach with respect to the localization accuracy except for a weak tendency for better accuracy with GFF. Considering the lower system complexity that is required for implementing GFF, even an equivalent level of accuracy can be regarded as an advantage for GFF. However, it must be noted that with GFF, a user can perform well only if the sensitivity and the resolution of the visual display are sufficiently high so that small variations in the reflected force become discernible.

The exploration time for GFF is considerably longer than for FF. This observation is justifiable given the fact that, with GFF, the subjects have to constantly refer to the visual display in order to detect a significant variation in the contact force profile, which corresponds to a lump. Therefore, although providing visual feedback about instrument/tissue interaction is useful for the purpose of lump localization, the corresponding task times are longer due to the need for cognitive processing by the users. This conclusion is consistent with previous results for teleoperation of nonsurgical tasks [21]. From the user's point of view, GFF's moderate need for human processing and interpretation may be a major drawback particularly for lengthy procedures or for dexterous tasks, in which the user has to keep track of several visual indicators and switch his/her attention between them without getting distracted from the main surgical task (sensory overload).

With regard to the energy supplied to the tissue by the users, the results are not consistently in favor of either GFF or FF. The higher levels of supplied energy under FF for two locations (out of five) seem to be a result of the fact that the localization ability under FF is proportional to the slave's velocity. In contrast, the slower the slave moves, the higher the localization ability will be under GFF.

V. Multimodal Contact Cues

Internet-based signal transmission and video streaming are increasingly becoming the technology of choice for a wide range of applications that include unilateral and bilateral teleoperation [23], [24]. In this method of transmission, the video quality can be easily affected by network congestion, which results in poor video quality at the human operator side [25].

Degraded visual conditions that are caused by internet protocol (IP) network impairments or other factors such as signal-to-noise degradation in wireless communication or depth perception difficulties in 2-D vision can make it difficult to prevent tissue damage in the absence of haptic sensation for the surgeon. In this section, we study the effects of visual, haptic, and graphical cues about tool/tissue interactions on user's performance for a typical surgical task. Whereas the inclusion of haptic feedback in a virtual-reality surgical simulator for a tissue holding task has been shown to help the user when visual feedback is impeded [26], our goal is to study how the graphical or haptic cues can effectively replace corrupted visual feedback in master–slave surgical teleoperation.

A. Case Study: Tissue Stiffness Discrimination Task

1) Experiment Design: Using the master–slave system, teleoperation experiments were conducted in which the task is to discriminate between any two soft tissues with different stiffnesses through telerobotic palpation. The motivation for studying this task is given by the fact that tissue palpation is one of the ways to detect cancerous tissue, which has a different stiffness compared to healthy tissue. Several contact feedback modalities are compared in terms of their capability in transmitting critical task-related information to the user.

In our experimental scenario, the visual link consisted of a 320×240 webcam-provided image, which is transmitted from the slave side to the master side via an H.323-based NetMeeting Internet videoconferencing application at a rate of 14 frames per second. The communication medium was a 1000T-base Ethernet network.

Six subjects (three males and three females) aged 24–34 participated in our experiments. The subjects had little to average exposure to haptic and visual cues and average experience with the master–slave system. The subjects' primary goal was defined as distinguishing between different tissues in terms of their relative stiffness. After a tissue sample was presented to the subject and probed, it was replaced with a different or the same tissue sample upon the subject's verbal signal. The subjects would also verbally signify the completion of the task.

The subjects received visual, haptic, graphical, or graphical plus haptic cues about the level of tool/tissue interactions forces as the tool indented the soft tissue (see Fig. 16). Since

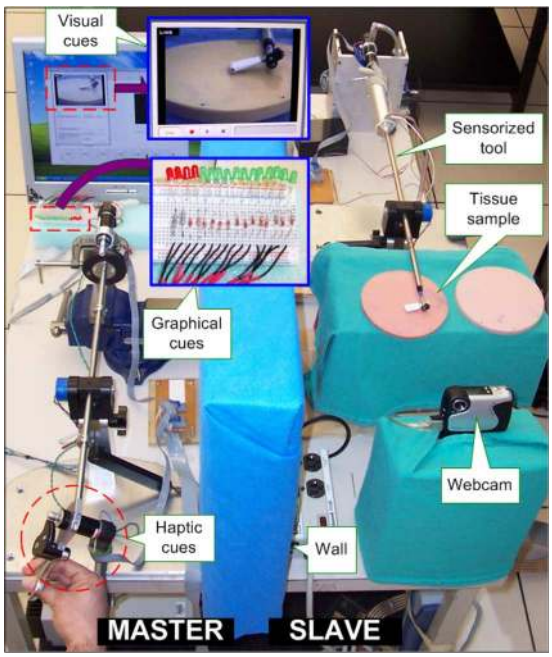

Fig. 16. Master–slave setup for performing telemanipulated tissue stiffness discrimination task.

our intention was to study the utility of haptic and graphical feedback under degraded or suppressed visual conditions, camera vision from the slave side was switched off when the subjects received haptic and/or graphical cues so that visual cues did not play a role.

In each trial, one out of the aforementioned four different feedback modalities and a combination of two out of three different tissue samples (two different tissues or the same tissue twice) were presented to the subject. In total, each subject made 16 trials (i.e., 16 combinations of feedback modality and tissue pair randomly selected out of the 24 possible combinations). The trials were presented in a randomized order to the subjects. Before the experiments, each subject was given three to four practice trials until he or she felt comfortable with the operation of the master–slave system. Each palpation trial started from orienting the master handle (the slave's end-effector) in vertical (horizontal) position followed by twisting the handle to explore the tissue (user's wrist rotation angle $\in [0,\ 90^\circ]$).

2) Results: The test results for the palpation task are shown in Fig. 17 in the form of bar graphs of mean values. Fig. 17(a) shows the trials' success rate for the four different feedback modes. As can be seen, graphical cueing is the most successful modality for tissue stiffness discrimination. To further investigate this, first, a one-way ANOVA test was applied to the success rate statistics of the feedback modes $(F(3, 92) = 1.426, p = 0.2401)$, which did not indicate a significant difference among the success rate statistics. Due to the pass/fail nature of the tests (1: successful; 0: unsuccessful) and for a more elaborate analysis, we used separate t-tests between different pairs of feedback modes. A two-tailed t-test between graphical and visual feedback modes $(t(24) = 1.163, p = 0.257)$ shows no significant difference. A two-tailed t-test between the visual and haptic modes indicates no significant difference $(t(24) = 2.069, p = 0.538)$. However, a right-tailed t-test between the graphical and haptic feedback modes $(t(24) = 1.813, p = 0.0415)$ indicates a higher success rate for graphical feedback compared to haptic feedback. Another two-tailed t-test between haptic and haptic plus graphical feedback modes showed them to be almost identical $(p > 0.5)$.

The bar graph of Fig. 17(b) represents the mean values of task completion times (in seconds) for different feedback modes. An ANOVA test for the four feedback modes $(F(3, 92) = 0.7627, p = 0.5178)$ shows that there is no significant difference among the average task times. However, a two-tailed t-test $(t(24) = 2.069, p = 0.0285)$ shows that the task completion times are longer under visual feedback than haptic feedback.

Fig. 17(c) shows the mean values of the energy that is supplied to the tissue (in joules) under the four feedback modes. This graph indicates that the haptic plus graphical mode (very closely followed by haptic mode) and the visual mode supplied the lowest and the highest energy to tissues, respectively. An ANOVA test confirms a significant difference between the haptic, graphical, and visual modes from the energy point of view ($F(2, 69) = 6.3806$, which corresponds to $p = 0.000241$, which, based on the 5% level of ruling for p values, implies significantly different mean energies). In order to further study the closeness of the mean supplied energy under the visual and graphical feedback modes, a right-tailed t-test $(t(24) = 2.247$, which corresponds to $p = 0.01725)$ shows that visual cues significantly supply higher energy to tissue. A two-tailed t-test $(t(24) = 2.069, p = 0.0037)$ confirms that the mean supplied energy for the visual mode is significantly higher than that for the haptic mode. A right-tailed t-test between the graphical and haptic modes $(t(24) = 2.069, p = 0.025)$ shows that the mean supplied energy for the graphical mode is significantly higher than that for the haptic mode. Finally, a right-tailed t-test between the haptic and the haptic plus graphical modes confirms that the null hypothesis $\mu_1 = \mu_2$ holds $(t(24) = 0.7355$, which corresponds to $p = 0.2347)$.

3) Discussion: After analyzing the results of the palpation trials, the following trends were observed.

Since a subject had to decide whether the two tissue samples were "similar," "the first one softer compared to the second one," and "the first one harder compared to the second one," the chance level was 33%. Therefore, all of the success rates are well above this chance level. As for the relative success rate of different feedback modalities, the results show that for a task involving the comparison of force/deformation tissue characteristics, graphical cueing is advantageous over haptic cueing. One reason for the superior performance that is achieved with graphical cues compared to haptic cues is that the sensitivity of a graphical force indicator is only limited by the resolution of the force measurements, whereas the sensitivity of haptic rendering is limited in nature (0.5 N or 7% is the just-noticeable difference for force sensing by the human hand) [27], [28]. The superiority of the graphical mode comes along with the benefit of simplicity of its implementation. On the downside, one should bear in mind that the domain of tasks that can benefit from graphical cues is not very extensive, as with increased task complexity/dexterity (e.g., increase in a task's number of DOFs), there can be a tremendous increase in the cognitive

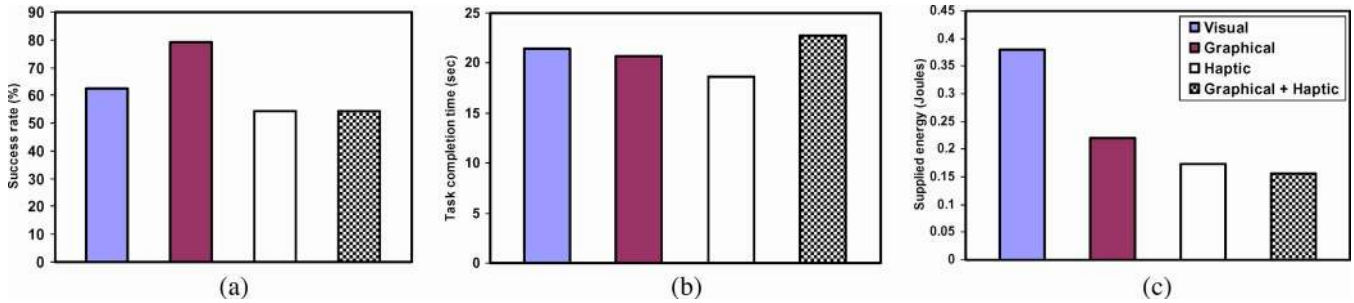

Fig. 17. (a) Mean success rate. (b) Mean completion time (in seconds). (c) Mean energy supplied to the tissue (in joules).

processing that is required by the user. An advantage of haptic cues is that they are intuitive and require the least amount of cognitive processing.

As for the success rate with visual cues, it was observed during the experiments that the depth of tissue indentation could not be precisely quantified by the subjects. Although this may make one expect the success rate to be significantly lower for visual cueing compared to graphical cueing, this was not corroborated by the two-tailed t-test—a fact that may be attributed to the relatively low number of trials (a total of 96 trials as a result of having 6 subjects and 16 trials per subject; an average of 24 trials per feedback modality). The success rate for visual cues strongly depends on the video's information content, which, in turn, can be attributed to various task-dependent and task-independent factors that range from network conditions for IP-based video streaming to the camera's angle of view. For example, task performance might be seriously degraded if critical movements of the task are orthogonal to the camera view, which causes depth perception problems. The close success rates for the visual and haptic modes show that haptic feedback can effectively replace a degraded visual cue.

Although one might have expected the graphical plus haptic mode to result in a significantly higher success rate compared to haptic feedback, this was not corroborated by the two-tailed t-test that was done. In practice, it was observed that during the subjects' simultaneous exposure to the haptic and graphical cues in this particular task, they had strong tendencies toward the haptic portion, which made the statistics quite similar to those of the pure haptic mode.

With respect to task completion time, haptic feedback performs better than visual feedback. Although one's expectation would be that haptic cues result in much shorter task times, in practice, this was not the case due to the fact that the tissue stiffnesses were not significantly different, and subjects needed to palpate each tissue usually more than once.

The worst performance in terms of supplying energy and consequently incurring damage/injury to tissue was provided by the visual cueing mode. The reason is that a subject had to supply a significant amount of energy before tissue deformations were quantifiable. As a result, the distance between the visual mode and the other modalities with respect to the supplied energy to tissue is quite noticeable. Therefore, the haptic mode can also effectively replace a corrupted visual cue from an energy point of view.

VI. Concluding Remarks and Future Directions

This paper studied the 2CH and 4CH bilateral teleoperation control architectures from both stability and transparency points of view. Using a haptics-capable master–slave testbed, it was found that slave/environment force measurements can significantly improve teleoperation transparency in a 2CH architecture. Unlike 2CH architectures, a sufficient number of design parameters in the 4CH architecture enable it to achieve ideal transparency. However, as a result of the stability-performance tradeoff, the stability of the ideally transparent 4CH system critically depends on the exact implementation of the control laws and having an exact model of the teleoperation system. On the other hand, local FF terms in the 4CH architecture can be used to increase the stability and performance robustness of the teleoperation system against nonidealities in bilateral control implementation. The theoretical results were experimentally validated. It was observed that the 3CH architecture provides optimum performance at a relatively low implementation cost and was therefore used as the haptic feedback scheme in the rest of this study. Next, for localization of a lump that is embedded in soft tissue, performance comparisons were made for situations in which haptic feedback is substituted by a graphical display of haptic information. It was observed that the localization accuracy is comparable for both feedback modalities, which means that in cases where a haptic user interface is not available, GFF can adequately and cost-effectively substitute for haptic feedback. However, this comes at the expense of longer task completion times for graphical feedback. Finally, we compared users' performance under visual, haptic, graphical, and graphical plus haptic feedback modalities for a soft-tissue palpation task. The goal was to study how the graphical or haptic cues can effectively replace a corrupted visual cue. It was found that graphical cueing and haptic cueing respectively lead to a higher and an equal rate of success in discriminating between two tissue samples with different stiffnesses compared to the visual mode, whereas the visual mode incurs the highest risk of tissue damage due to excessive tissue deformation.

As a future work, we will perform human factors studies to compare users' performance for surgical tasks when the users receive haptic or graphical feedback in the presence of master–slave communication latency. This will help us assess the effectiveness of 2CH time-delay compensation methods versus their 4CH counterparts [29]. The outcome of this research will also answer an important question, which is whether

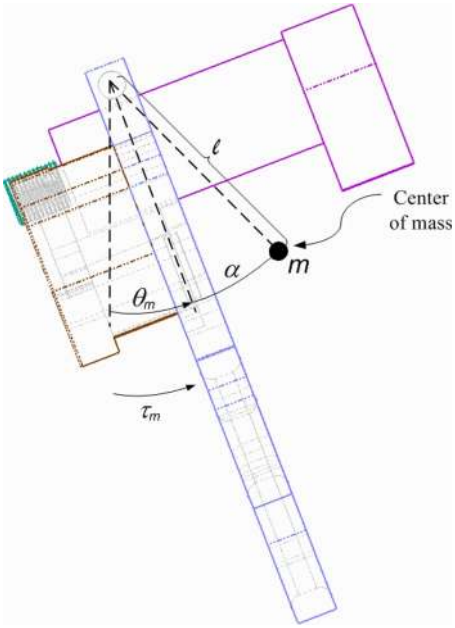

Fig. 18. Master handle.

haptic feedback is useful in the presence of time delay or confuses the user to the point that it does not serve any useful purpose.

APPENDIX A
MASTER SYSTEM MODELING AND IDENTIFICATION

A. Dynamic Modeling

The one DOF dynamic model of the master in the twist direction

$$\tau_m = (m\ell^2 + I_{zz})\ddot{\theta}_m + mg\ell\sin(\theta_m + \alpha) \tag{35}$$

is needed for implementing the bilateral control laws that are discussed in the paper. Here, as shown in Fig. 18, τ_m and θ_m are the joint torque and angular position at the motor output shaft, respectively. The center of mass m of the master is located at a distance ℓ and an angle α with respect to the master's axis of rotation. I_{zz} is the master's mass moment of inertia with respect to the axis of rotation.

Consider two rigid bodies that make contact through elastic bristles, then, the friction force/torque τ_{fric} between the two can be modeled based on their relative velocity $\dot{\theta}$ and the bristles's average deflection z as [30]

$$\frac{dz}{dt} = \dot{\theta} - \sigma_0 \frac{|\dot{\theta}|}{s(\dot{\theta})} z \tag{36}$$

$$\tau_{\text{fric}} = \sigma_0 z + \sigma_1 \frac{dz}{dt} + \sigma\dot{\theta} \tag{37}$$

where σ_0 and σ_1 are the stiffness and damping parameters for the friction dynamics, respectively, and the term $\sigma\dot{\theta}$ accounts for the viscous friction. Using the Stribeck term $s(\dot{\theta}) = \tau_c(1 - e^{-a|\dot{\theta}|}) + \tau_s e^{-a|\dot{\theta}|}$, where τ_c and τ_s are the Coulomb and stiction frictions, respectively, friction can be written as

$$\tau_{\text{fric}} = \sigma\dot{\theta} + \tau_c\left(1 - e^{-a|\dot{\theta}|}\right)\text{sgn}(\dot{\theta}) + \tau_s e^{-a|\dot{\theta}|}\text{sgn}(\dot{\theta}). \tag{38}$$

For the master device, assuming asymmetry in Stribeck friction effects when the master moves in the positive and negative directions, the dynamics can be written as

$$\begin{aligned}\tau_m = {} & M_m\ddot{\theta}_m + G\sin(\theta_m + \alpha) + \sigma\dot{\theta}_m \\ & + \tau_{c_1}\left(1 - e^{-a_1|\dot{\theta}_m|}\right)u_{\dot{\theta}_m} + \tau_{s_1}e^{-a_1|\dot{\theta}_m|}u_{\dot{\theta}_m} \\ & + \tau_{c_2}\left(1 - e^{-a_2|\dot{\theta}_m|}\right)u_{-\dot{\theta}_m} + \tau_{s_2}e^{-a_2|\dot{\theta}_m|}u_{-\dot{\theta}_m}\end{aligned} \tag{39}$$

where τ_{c_i}, τ_{s_i}, and a_i correspond to the positive direction ($\dot{\theta}_m > 0$) for $i = 1$ and to the negative direction ($\dot{\theta}_m < 0$) for $i = 2$, and $u(\cdot)$ is the unity step function.

B. Parametric Identification

The master dynamics (39) are unknown in terms of rigid-body parameters for inertia and gravity M_m, G, α, and in friction parameters σ, τ_{c_1}, τ_{s_1}, a_1, τ_{c_2}, τ_{s_2}, and a_2. To identify these parameters, sinusoidal input torques with different amplitudes and frequencies were provided to the master. Using the obtained joint torque, position, velocity, and acceleration data, a nonlinear multivariable minimization procedure (Matlab function *fminimax*) was used to find the parameter estimates that best fit the dynamic model (39): $M_m = 5.97 \times 10^{-4}$ kg · m^2, $G = 1.04 \times 10^{-1}$ N · m, $\alpha = 9.3965°$, $\sigma = 6.88 \times 10^{-4}$ N · m s/rad, $\tau_{c_1} = 1.98 \times 10^{-2}$ N · m, $\tau_{s_1} = 0$ N · m, $a_1 = 55.2$ s/rad, $\tau_{c_2} = -1.62 \times 10^{-2}$ N · m, $\tau_{s_2} = 0$ N · m, and $a_2 = 42.1$ s/rad. The above-identified parameters were used to compensate for the gravity and friction effects, thus simplifying the dynamic model of the master to $\tau_m = M_m\ddot{\theta}_m$.

APPENDIX B
t-TEST AND ANOVA

Given two paired sets x_i and y_i of n measured values, the paired t-test determines whether they differ from each other in a significant way under the assumptions that the paired differences are independent and identically normally distributed. To apply the test, let $\hat{x}_i = (x_i - \bar{x})$ and $\hat{y}_i = (y_i - \bar{y})$, then, t is defined by

$$t = (\bar{x} - \bar{y})\sqrt{\frac{n(n-1)}{\sum_{i=1}^{n}(\hat{x}_i - \hat{y}_i)^2}}. \tag{40}$$

A table of Student's t-distribution confidence intervals can be used to determine the significance level at which two distributions differ.

Similar to the two-sample t-test, ANOVA provides the means for testing hypotheses about the mean (average) of a dependent variable across different groups. Whereas the t-test is used to compare the means between two groups, one-way ANOVA is

used when the study involves three or more levels of a single independent variable. The ANOVA test procedure produces an F-statistic, which is used to test the statistical significance of the differences among the obtained means of two or more random samples from a given population (p value).

REFERENCES

[1] D. Repperger, C. Phillips, J. Berlin, A. Neidhard-Doll, and M. Haas, "Human–machine haptic interface design using stochastic resonance methods," *IEEE Trans. Syst., Man, Cybern. A, Syst., Humans*, vol. 35, no. 4, pp. 574–582, Jul. 2005.

[2] C. Wagner, N. Stylopoulos, and R. Howe, "The role of force feedback in surgery: Analysis of blunt dissection," in *Proc. 10th Symp. Haptic Interfaces Virtual Environ., Teleoperator Syst.*, Orlando, FL, 2002, pp. 68–74.

[3] G. Tholey, J. P. Desai, and A. E. Castellanos, "Force feedback plays a significant role in minimally invasive surgery: Results and analysis," *Ann. Surg.*, vol. 241, no. 1, pp. 102–109, Jan. 2005.

[4] J. P. Ruurda, I. A. Broeders, B. Pulles, F. M. Kappelhof, and C. van der Werken, "Manual robot assisted endoscopic suturing: Time-action analysis in an experimental model," *Surg. Endosc.*, vol. 18, no. 8, pp. 1249–1252, Aug. 2004.

[5] P. Joice, G. B. Hanna, and A. Cuschieri, "Errors enacted during endoscopic surgery—A human reliability analysis," *Appl. Ergon.*, vol. 29, no. 6, pp. 409–414, Dec. 1998.

[6] M. Tavakoli, R. Patel, and M. Moallem, "Haptic interaction in robot-assisted endoscopic surgery: A sensorized end effector," *Int. J. Med. Robot. Comput. Assist. Surg.*, vol. 1, no. 2, pp. 53–63, 2005.

[7] G. Tholey and J. Desai, "On-site three dimensional force sensing capability in a laparoscopic grasper," *Ind. Robot: Int. J.*, vol. 31, no. 6, pp. 509–518, 2004.

[8] E. J. Stephenson, S. Sankholkar, C. T. Ducko, and R. J. J. Damiano, "Robotically assisted microsurgery for endoscopic coronary artery bypass grafting," *Ann. Thorac. Surg.*, vol. 66, no. 3, pp. 1064–1067, Sep. 1998.

[9] D. A. Lawrence, "Stability and transparency in bilateral teleoperation," *IEEE Trans. Robot. Autom.*, vol. 9, no. 5, pp. 624–637, Oct. 1993.

[10] B. Hannaford, "A design framework for teleoperators with kinesthetic feedback," *IEEE Trans. Robot. Autom.*, vol. 5, no. 4, pp. 426–434, Aug. 1989.

[11] S. Haykin, *Active Network Theory*. Reading, MA: Addison-Wesley, 1970.

[12] K. B. Fite, L. Shao, and M. Goldfarb, "Loop shaping for transparency and stability robustness in bilateral telemanipulation," *IEEE Trans. Robot. Autom.*, vol. 20, no. 3, pp. 620–624, Jun. 2004.

[13] Y. Yokokohji and T. Yoshikawa, "Bilateral control of master–slave manipulators for ideal kinesthetic coupling-formulation and experiment," *IEEE Trans. Robot. Autom.*, vol. 10, no. 5, pp. 605–620, Oct. 1994.

[14] J. E. Colgate, "Robust impedance shaping telemanipulation," *IEEE Trans. Robot. Autom.*, vol. 9, no. 4, pp. 374–384, Aug. 1993.

[15] H. Kazerooni, "Human–robot interaction via the transfer of power and information signals," *IEEE Trans. Syst., Man, Cybern.*, vol. 20, no. 2, pp. 450–463, Mar./Apr. 1990.

[16] K. Hashtrudi-Zaad and S. E. Salcudean, "Transparency in time delay systems and the effect of local force feedback for transparent teleoperation," *IEEE Trans. Robot. Autom.*, vol. 18, no. 1, pp. 108–114, Feb. 2002.

[17] M. Tavakoli, R. V. Patel, and M. Moallem, "Bilateral control of a teleoperator for soft tissue palpation: Design and experiments," in *Proc. IEEE Int. Conf. Robot. Autom.*, 2006, pp. 3280–3285.

[18] M. Tavakoli, R. Patel, and M. Moallem, "A haptic interface for computer-integrated endoscopic surgery and training," *Virtual Real.*, vol. 9, no. 2/3, pp. 160–176, Jan. 2006.

[19] S. Nicosia and P. Tomei, "Robot control by using only joint position measurements," *IEEE Trans. Autom. Control*, vol. 35, no. 9, pp. 1058–1061, Sep. 1990.

[20] L. N. Verner and A. M. Okamura, "Sensor/actuator asymmetries in telemanipulators: Implications of partial force feedback," in *Proc. 14th Symp. Haptic Interfaces Virtual Environ., Teleoperator Syst.*, New York, 2006, pp. 309–314.

[21] M. Massimino, "Sensory substitution for force feedback in teleoperation," Ph.D. dissertation, MIT, Cambridge, MA, 1992.

[22] M. Kitagawa, D. Dokko, A. M. Okamura, and D. D. Yuh, "Effect of sensory substitution on suture manipulation forces for robotic surgical systems," *J. Thorac. Cardiovasc. Surg.*, vol. 129, no. 1, pp. 151–158, Jan. 2005.

[23] X.-G. Wang, M. Moallem, and R. V. Patel, "An Internet-based distributed multiple-telerobot system," *IEEE Trans. Syst., Man, Cybern. A, Syst., Humans*, vol. 33, no. 5, pp. 627–633, Sep. 2003.

[24] I. Polushin, P. Liu, and C.-H. Lung, "A control scheme for stable force-reflecting teleoperation over IP networks," *IEEE Trans. Syst., Man, Cybern. B, Cybern.*, vol. 36, no. 4, pp. 930–939, Aug. 2006.

[25] D. Wu, Y. T. Hou, W. Zhu, Y. Q. Zhang, and J. M. Peha, "Streaming video over Internet: Approaches and directions," *IEEE Trans. Circuits Syst. Video Technol.*, vol. 11, no. 3, pp. 282–300, Mar. 2001.

[26] R. McColl, I. Brown, C. Seligman, F. Lim, and A. Alsaraira, "Haptic rendering and perception studies for laparoscopic surgery simulation," in *Proc. 28th IEEE Eng. Med. Biol. Conf.*, New York, 2006, pp. 833–836.

[27] K. Shimoga, "A survey of perceptual feedback issues in dextrous telemanipulation: Part I. Finger force feedback," in *Proc. IEEE Annu. Virtual Reality Int. Symp*, Seattle, WA, 1993, pp. 263–270.

[28] G. Campion and V. Hayward, "Fundamental limits in the rendering of virtual haptic textures," in *Proc. 1st Joint Eurohaptics Conf. Haptic Interfaces Virtual Environ., Teleoperator Syst.*, Pisa, Italy, 2005, pp. 263–270.

[29] A. Aziminejad, M. Tavakoli, R. Patel, and M. Moallem, "Wave-based time delay compensation in bilateral teleoperation: Two-channel versus four-channel architectures," in *Proc. Amer. Control Conf.*, New York, 2007, pp. 1449–1454.

[30] C. C. de Wit, H. Olsson, K. J. Astrom, and P. Lischinsky, "A new model for control of systems with friction," *IEEE Trans. Autom. Control*, vol. 40, no. 3, pp. 419–425, Mar. 1995.

Mahdi Tavakoli received the M.Sc. degree in electrical engineering from K. N. Toosi University of Technology, Tehran, Iran, in 1999 and the Ph.D. degree in electrical and computer engineering from the University of Western Ontario, London, ON, Canada, in 2005.

He is currently a Postdoctoral Fellow with the BioRobotics Laboratory of the School of Engineering and Applied Sciences, Harvard University, Cambridge, MA. His research interests are in haptic teleoperation, image-guided robotic surgery, and identification and control of dynamical systems.

Dr. Tavakoli was awarded an Ontario Graduate Scholarship in Science and Technology in 2004 and is a recipient of a Post-Doctoral Fellowship from the Natural Sciences and Engineering Research Council of Canada in 2007–2008.

Arash Aziminejad received the M.Sc. and Ph.D. degrees in electrical engineering from Iran University of Science and Technology, Tehran, Iran, in 1997 and 2003, respectively. He is currently working toward the Ph.D. degree at the University of Western Ontario, London, ON, Canada.

His research interests are in wireless telecommunications, cellular systems, robotics, and control systems, particularly bilateral teleoperation, passivity-based control, and time-delay compensation.

Dr. Aziminejad is a recipient of the Ontario Graduate Scholarship and the Ontario Graduate Scholarship in Science and Technology.

Rajni V. Patel received the B.Eng. degree in electronics with First Class Honors from the University of Liverpool, Liverpool, U.K., in 1969, and the Ph.D. degree in electrical engineering from the University of Cambridge, Cambridge, U.K., in 1973.

From 1973 to 1998, he held postdoctoral and faculty positions with the University of Cambridge; Lund Institute of Technology, Sweden; NASA Ames Research Center, USA; University of Waterloo, Waterloo, ON, Canada; Delft University of Technology, Delft, The Netherlands; the Control Systems Centre, UMIST, England; and Concordia University, Montreal, QC, Canada. At present, he is currently the Distinguished University Professor and Tier-1 Canada Research Chair in Advanced Robotics with the Department of Electrical and Computer Engineering, University of Western Ontario, London, ON. He also serves as a Director of Engineering with Canadian Surgical Technologies and Advanced Robotics, a research program of the London Health Sciences Centre, the Lawson Health Research Institute, and the University of Western Ontario. He has published over 300 papers in refereed journals and conferences in the areas of robotics (including medical and surgical robotics), haptics, systems and control, artificial neural networks, and mechatronics. He has coauthored a textbook and seven research monographs on robotics and control, and coedited an IEEE Press Reprint Book on *Numerical Linear Algebra Techniques for Systems and Control*. He has served as an editor for the *Journal of the International Federation of Automatic Control*, and is currently a member of the Advisory Board of the *International Journal of Medical Robotics and Computer Assisted Surgery*.

Dr. Patel is a Fellow of the American Society of Mechanical Engineers (ASME). In 2007, he was awarded the Hellmuth Prize for Achievement in Research by the University of Western Ontario. He has served on the editorial boards of the IEEE/ASME TRANSACTIONS ON MECHATRONICS, and the IEEE TRANSACTIONS ON ROBOTICS, and the IEEE TRANSACTIONS ON AUTOMATIC CONTROL, *Automatica*. He is a registered Professional Engineer in the province of Ontario, Canada.

Mehrdad Moallem received the Ph.D. degree in electrical and computer engineering from Concordia University, Montreal, QC, Canada, in 1997.

From 1998 to 1999, he was a Research and Development Engineer with Duke University, Durham, NC. From 1999 to 2007, he was an Assistant and then an Associate Professor with the Department of Electrical and Computer Engineering, University of Western Ontario, London, ON, Canada. He is currently an Associate Professor with the School of Engineering, Simon Fraser University, Burnaby, BC, Canada. His research interests include mechatronics, robotics, control applications, and embedded systems.